ATLAS CONF Note

STDM-2022-046

8th July 2022

Study of $Z \rightarrow ll\gamma$ decays at $\sqrt{s} = 8$ TeV in the ATLAS experiment at the LHC

The ATLAS Collaboration

This note presents a study of $Z \rightarrow ll\gamma$ decays in the ATLAS experiment at the Large Hadron Collider. The analysis uses a proton–proton data sample corresponding to an integrated luminosity of 20.2 fb^{-1} collected at a centre-of-mass energy $\sqrt{s} = 8$ TeV. Integrated fiducial cross-sections together with normalised differential fiducial cross-sections, sensitive to the kinematics of final-state QED radiation, are obtained. The results are found to be in agreement with state-of-the-art predictions for final-state QED radiation. First measurements of $Z \rightarrow ll\gamma\gamma$ decays are also reported.

1 Introduction

The production and decay of Z bosons to lepton pairs at the Large Hadron Collider (LHC) through the Drell-Yan mechanism has been a topic of very fruitful and detailed studies in the LHC experiments and the precision of the measurements has also led over the past decade to impressive theoretical developments, mostly in the area of higher-accuracy quantum chromodynamic (QCD) predictions.

Precise predictions for quantum electrodynamic and electroweak (QED/EW) effects are also of prime importance for key measurements at the LHC, such as that of the W-boson mass or of the weak mixing angle: this became very clear already at the end of the run-1 data-taking period [1, 2]. The analysis described in this note focuses on the final-state radiation of photons in Drell-Yan production of Z bosons decaying to an electron or muon pair. This process, denoted in the following as QED FSR, can be calculated separately from QED initial-state radiation (ISR) and from initial-final-state interference (IFI) thanks to gauge invariance. Owing to the narrow width of the Z boson and to the kinematic selections applied to the final state particles, the contributions from QED ISR and QED IFI in the fiducial phase space of the measurements described below are expected to be very small.
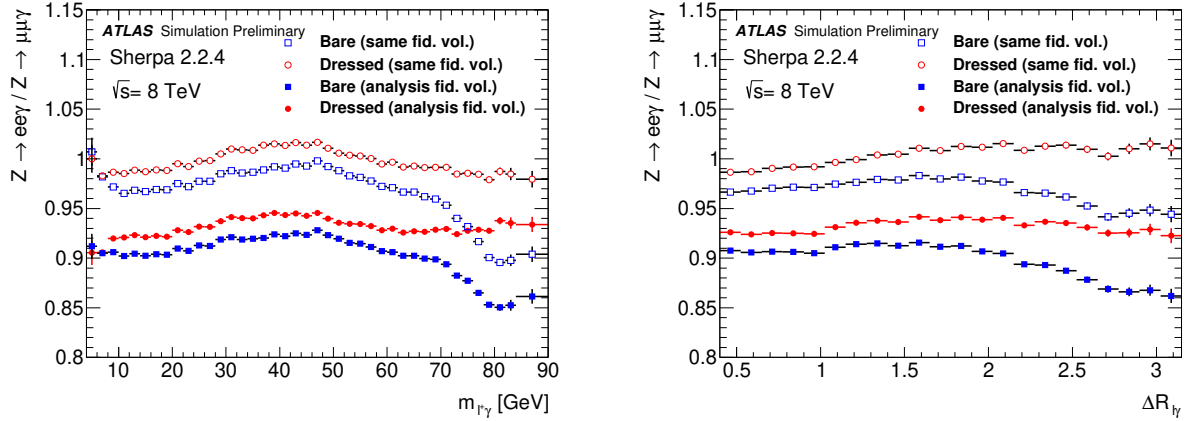

Figure 1: Predicted ratios of expected differential cross-sections for the invariant mass, $m_{l^+\gamma}$, of the positively charged lepton and the photon (left) and of the angle, $\Delta R_{l\gamma}$, between the photon and the closer of the two leptons (right) for electrons compared to muons. The ratios are shown for the bare and dressed lepton definitions described in the text. The predictions are obtained from a high-statistics inclusive Z-boson sample using Sherpa 2.2.4 and are shown for events containing two high-p_T leptons and one high-p_T photon satisfying the fiducial volume selections described in Table 2 in Section 6 (full symbols). Since most of the difference between electrons and muons observed in this case for the bulk of the distributions is due to the higher acceptance in η for the muons, the electron to muon ratios are also shown in the case of identical fiducial selections for both charged leptons (open symbols).

When considering QED radiation, fixed-order partitioning of the calculations has been shown at the time of the large electron-positron collider (LEP) to be sub-optimal in terms of obtaining the most precise predictions. Photon resummation techniques using exponentiation, as in KKMC [3], Photos [4] and Yennie-Frautschi-Suura (YFS) [5] were therefore developed for QED FSR, and then expanded to be used also for QED ISR and for physics at the LHC. This analysis uses specific configurations of Powheg+Pythia [6–9] with Photos and of Sherpa [10, 11] with YFS, as described in Section 3. These Monte-Carlo (MC) tools provide complete simulated events at LHC energies, in which the final state frequently contains several soft/collinear photons near the final-state leptons from the Z-boson decay, in

addition to the single hard large-angle photon emission required by the analysis selection described in Section 4. As discussed in Section 8, the measurement results presented in this note cover normalised fiducial differential cross-sections and integrated cross-sections for $Z \rightarrow ll\gamma$ decays and a first measurement of $Z \rightarrow ll\gamma\gamma$ decays.

One often labels the leptons in such final-state configurations as "bare" leptons, a notation adopted throughout this note, even though the meaning of such a bare lepton is by definition dependent on the tool used to describe multiple-photon emissions in QED FSR. One can also define a "dressed" lepton by combining the bare four-momenta of each lepton with that of QED FSR photons collected close to the lepton within a cone of size $\Delta R = 0.1$ around it.

Since soft/collinear QED emissions are regularised by the lepton mass, the predictions for the kinematic observables describing the final state will differ significantly in some regions of phase space between bare electrons and bare muons. This is shown in the case of predictions from Sherpa 2.2.4 [11] in Fig. 1 for the shape of the normalised distribution for the invariant mass, $m_{l^+\gamma}$, of the positively charged lepton and the photon and for the angle, $\Delta R_{l\gamma}$, between the photon and the closer of the two leptons. For large values of $m_{l^+\gamma}$, which are close to the edge of the phase space available for $Z \rightarrow ll\gamma$ decays and for large values of $\Delta R_{l\gamma}$, which correspond to specific configurations of $Z \rightarrow ll\gamma$ decays where the dilepton pair and the photon are back-to-back, Fig. 1 shows that one expects about 5% less $Z \rightarrow ee\gamma$ decays than $Z \rightarrow \mu\mu\gamma$ decays relative to the bulk of the distribution. It should be noted that most of the difference between electrons and muons observed in these plots for the bulk of the distributions is due to the higher acceptance in η for the muons (see Table 2).

Figure 1 also shows that the dressed lepton definition minimises the differences between electrons and muons. The use of dressed leptons also minimises the impact of the QED FSR radiation on the integrated cross sections. It is often used for exclusive analyses of e.g. Z/W+jet production because it unambiguously assigns the QED FSR photons to the leptons rather than to hadronic jets when performing such exclusive measurements. However, it is not optimal for precise studies of the QED FSR radiation itself.

For the purpose of the analysis described in this note, all results presented in Section 8 are shown separately for bare electrons and muons with the exception of the low-statistics measurement of $Z \rightarrow ll\gamma\gamma$ final states described in Section 9, in which bare electrons and muons are combined.

2 The ATLAS detector

The ATLAS experiment [12] at the LHC is a multipurpose particle detector with a forward–backward symmetric cylindrical geometry and a near 4π coverage in solid angle.[1] It consists of an inner tracking detector surrounded by a thin superconducting solenoid providing a 2 T axial magnetic field, electromagnetic and hadron calorimeters, and a muon spectrometer. The inner tracking detector covers the pseudorapidity range $|\eta| < 2.5$. It consists of silicon pixel, silicon microstrip, and transition radiation tracking detectors. Lead/liquid-argon (LAr) sampling calorimeters provide electromagnetic (EM) energy measurements with high granularity. A steel/scintillator-tile hadron calorimeter covers the central pseudorapidity range

---

[1] ATLAS uses a right-handed coordinate system with its origin at the nominal interaction point (IP) in the centre of the detector and the z-axis along the beam pipe. The x-axis points from the IP to the centre of the LHC ring, and the y-axis points upwards. Cylindrical coordinates (R, ϕ) are used in the transverse plane, ϕ being the azimuthal angle around the z-axis. The pseudorapidity is defined in terms of the polar angle θ as $\eta = -\ln\tan(\theta/2)$. Angular distance is measured in units of $\Delta R \equiv \sqrt{(\Delta\eta)^2 + (\Delta\phi)^2}$.

($|\eta| < 1.7$). The end-cap and forward regions are instrumented with LAr calorimeters for both the EM and hadronic energy measurements up to $|\eta| = 4.9$. The muon spectrometer surrounds the calorimeters and is based on three large superconducting air-core toroidal magnets with eight coils each. The field integral of the toroids ranges between 2.0 and 6.0 T m across most of the detector. The muon spectrometer includes a system of precision tracking chambers and fast detectors for triggering. A three-level trigger system is used to select events to be recorded. The first-level trigger is implemented in hardware and uses a subset of the detector information to accept events at a rate of at most 75 kHz. This is followed by two software-based trigger levels that together reduce the accepted event rate to 400 Hz on average depending on the data-taking conditions during 2012.

3 Data and simulated event samples

The data used in this analysis was collected in 2012 using pp collisions at a centre-of-mass energy of 8 TeV. The corresponding total integrated luminosity is 20.2±0.4 fb^{-1}. The average number of inelastic pp interactions produced per bunch crossing for this dataset is 20.7.

The Powhegbox v1 Monte Carlo (MC) programme [6–9] was used for the simulation of Z-boson decays at next-to-leading order (NLO) in QCD using the CTEQ6L1 PDF set [13]. It was interfaced to Pythia8 [14] for the modelling of the parton shower, hadronisation, and underlying event, with parameters set according to the AU2 CT10 tune [15]. QED FSR is modelled using the exponentiated multi-photon emission provided by Photos [16]. This combination of MC tools, denoted Powheg+Pythia8+Photos is used as the main MC sample to estimate the effects of detector efficiency and resolution and to unfold the data presented in this note. Initial-state radiation of photons (QED ISR) and initial-final-state interference (IFI) are not included in the simulation. For QED FSR photons, Photos is configured to include a matrix-element correction for Z-boson decay which brings it very close (better than 10^{-3}) to NNLO QED accuracy [4] for the emission of up to two photons.

An alternative prediction for $pp \rightarrow ll\gamma$ production with up to three additional parton emissions at leading order in the strong coupling is provided by Sherpa 1.4.1 [10] using the CT10 PDF set [17]. Sherpa 1.4.1 is configured such that the leading photon is generated at matrix-element level with leading-order accuracy. Both FSR and ISR emissions are included in the simulation (but not the small effects expected from IFI). The YFS [5] approach is then used to exponentiate the radiation in a way similar to that done in Photos. The results obtained by using Sherpa 1.4.1 are compared to those obtained by using Powheg+Pythia8+Photos for a cross-check of the systematics related to the unfolding procedure. A specific version of Sherpa 1.4 (labelled Sherpa 1.4 ME$_{\gamma\gamma}$) containing an exact description at tree level of the production of lepton pairs accompanied by two hard photons has also been used to compare its predictions to the unfolded $Z \rightarrow ll\gamma\gamma$ measurements.

For the comparisons between predictions and the unfolded data, additional generator-level predictions for $pp \rightarrow ll\gamma$ production have been produced using Sherpa 2.2.4 [11] and KKMChh [18, 19]. The QED treatment in Sherpa 2.2.4 is identical to that described above for Sherpa 1.4.1, while the QCD treatment is more advanced [20]. KKMChh is an event generator for Z boson production and decays, which includes exponentiated multi-photon initial and final state radiation and virtual electroweak corrections. It separates the expected dominant contribution from QED FSR to the measurements presented in this note from the negligible contributions from QED ISR and QED IFI.

To minimise the impact of differences in the QCD aspects on the measurements of QED FSR differential spectra, the MC predictions for which data and MC are not expected to agree to better than 0.5% are all reweighted to the data. This procedure is clearly necessary for the p_T^Z spectrum which is only predicted at leading order in QCD for the two main MC samples produced for the analysis, but other distributions have also been studied to assess as precisely as possible the residual systematic uncertainties from the QCD aspects of the simulation in the measurements. This reweighting procedure is also applied to the MC predictions at generator level from Sherpa 2.2.4 and from KKMC-hh used to compare the unfolded results to the most accurate predictions available.

Background contributions from top-quark production ($t\bar{t}$, Wt, and t-channel single top production) are generated using Powhegbox with the CT10 PDF in conjunction with Pythia6 [14] (v6.427 using the CTEQ6L1 PDF) with the Perugia 2011C tune for parton showering, hadronisation, and underlying event. Background contributions from Z+jet and $Z \rightarrow \tau\tau$ production have been simulated using Sherpa 1.4.3 [10] with its default tune and the CT10 PDFs.

The simulated samples were processed through a full ATLAS detector simulation [21], based on GEANT4 [22], and reconstructed with the same software as that used for the data. All MC samples are corrected with data-driven correction factors to account for small differences in photon and lepton trigger, reconstruction, identification and isolation efficiencies between data and simulation. Additional $p-p$ interactions (pile-up), occurring in the same and neighbouring bunch crossings are simulated and overlaid at the detector hit level on top of the hard-scattering process from the MC simulation.

4 Selection of $Z \rightarrow ll\gamma$ events

The $Z \rightarrow ll\gamma$ candidate is formed by selecting the opposite-sign same-flavour dilepton pair with mass closest to m_Z and the highest p_T photon in the event. No explicit requirements are made on the presence or absence of other activity in the event, such as additional photons or leptons or jets. Background events from processes producing fake or non-prompt photons/leptons are suppressed by the lepton/photon identification criteria described below, including in particular isolation requirements on both leptons and on the photon.

Event candidates in both data and MC simulation are required to have fired at least one unprescaled single lepton or dilepton trigger, with a lowest p_T threshold of 24 GeV for single leptons and of 12-13 GeV for dilepton triggers. The single lepton triggers provide a high trigger efficiency with respect to the offline selection, which requires at least one lepton with p_T >25 GeV. The trigger efficiency for $Z \rightarrow ll\gamma$ events satisfying all the selection criteria described below is about 99%.

4.1 Photon and lepton selection

Photon and electron candidates are reconstructed [23] from clusters of energy deposits in the electromagnetic calorimeter combined with information from charged tracks reconstructed in the inner detector. Electrons and photons are identified by shower shape and hadronic leakage variables. Photons are required to satisfy all the requirements on shower-shape variables corresponding to the *Tight* photon identification criteria of [23]. Electron candidates are required to satisfy the *Loose* likelihood requirement of [23],

Photon (resp. electron) candidates are required to have a transverse momentum above 15 GeV (resp. 10 GeV) and a pseudorapidity in the range $|\eta| < 2.37$ (resp. $|\eta| < 2.47$). For the photon candidates, the transition region between the barrel and end-cap electromagnetic calorimeters, $1.37 < |\eta| < 1.52$, is excluded.

Muon candidates are reconstructed [24] from combined tracks in the inner detector and muon spectrometer with a transverse momentum above 10 GeV over the pseudorapidity range $|\eta| < 2.5$. Over the range $2.5 < |\eta| < 2.7$, stand-alone muon candidates in the muon spectrometer are used, based on tracks with reconstructed segments in three spectrometer stations.

Electron and muon candidates are required to originate from the appropriate primary vertex (each primary vertex candidate is reconstructed from at least two associated tracks with $p_T > 0.4$ GeV). The significance of the transverse impact parameter, defined as the absolute value of the track transverse impact parameter, d_0, measured relative to the beam trajectory, divided by its uncertainty, σ_{d_0}, must satisfy $|d_0|/\sigma_{d_0} < 5$ for electrons and $|d_0|/\sigma_{d_0} < 3$ for muons. The longitudinal impact parameter is required to satisfy $|z_0| < 10$ mm.

The photon, electron, and muon candidates are required to be isolated from other particles using selections based on calorimeter isolation. The calorimeter isolation is defined as the sum of the calorimeter cell transverse energies, $\sum E_T$, inside an isolation cone of $\Delta R = 0.2$ around the lepton or photon [25], while the track isolation is defined as the sum of the scalar transverse momenta of tracks with $p_T > 1$ GeV. In the case of the calorimeter isolation for photons/electrons, the cells corresponding to the calorimeter cluster itself are excluded from the sum. In addition, the calorimeter isolation is corrected on an event-by-event basis for the energy deposited by the photon or lepton candidate, and, using the method described in Refs. [26–28], for the contribution from the underlying event and pile-up. Each photon/electron (muon) is required to have a normalised calorimeter isolation smaller than 0.3 (0.2). Finally, photons close to leptons are excluded if $\Delta R_{l\gamma} < 0.4$.

4.2 Signal region definition

Candidate $Z \to ll\gamma$ signal events are selected by requiring that they contain at least one pair of opposite-charge, same-flavour leptons and at least one photon candidate. The highest-p_T lepton is required to have $p_T > 25$ GeV, while the second lepton must have $p_T > 10$ GeV. The selected dilepton pair in the event is that which has an invariant mass, $m_{ll\gamma}$, closest to m_Z. Only 2% of the events have more than one dilepton combination.

To further improve the purity of the QED FSR sample, the invariant mass of the dilepton pair, m_{ll}, is required to be between 20 and 80 GeV, while the three-body invariant mass, $m_{ll\gamma}$, is required to be between 80 and 100 GeV. These selections suppress mainly the background from Z-boson+jet production with a jet misidentified as a photon, which can be clearly seen in Fig. 2 outside the signal region. For similar reasons, these selections also reduce considerably the background from QED ISR. The integrated fiducial cross-section results are also extracted for a stricter selection on the invariant mass of the dilepton, $m_{ll} > 45$ GeV.

The criteria described above were applied to the 2012 data, leading to 30571 (resp. 34948) events selected in the $Z \to ee\gamma$ (resp. $Z \to \mu\mu\gamma$) channel (see Table 1 and Section 5 for more details). The reconstructed differential distributions are shown in Fig. 3 for the three observables of interest, the invariant mass of the positively charged lepton and the photon, $m_{l^+\gamma}$, the ΔR between the photon and the closer of the two leptons, $\Delta R_{l\gamma}$, and the transverse momentum of the photon, p_T^γ.
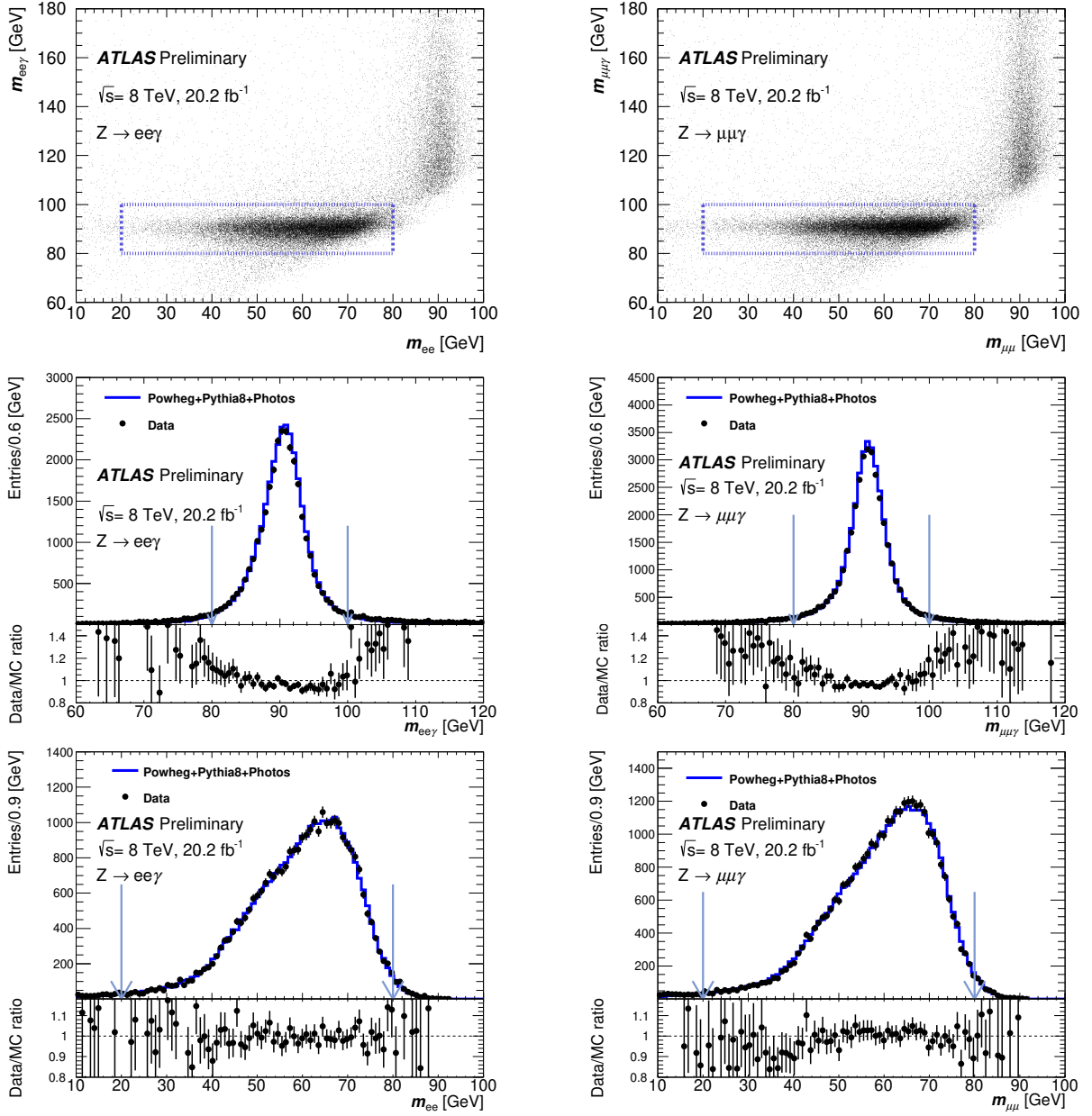
Figure 2: For $Z \to ee\gamma$ (left) and $Z \to \mu\mu\gamma$ (right) decay candidates in data, distribution of the three-body invariant mass, $m_{ll\gamma}$, versus the dilepton mass, m_{ll}. The dashed lines indicate the selection criteria applied in the analysis to these two reconstructed invariant masses. These criteria minimise in particular the background from Z bosons produced in association with jets in which one jet is misidentified as a photon. Also shown are the projections of these figures onto the vertical (middle plot with only the selection on m_{ll} applied) and horizontal (bottom plot with only the selection on $m_{ll\gamma}$ applied) axes with the corresponding vertical lines indicating the selection cuts described above. The curves show the signal predictions from the nominal Powheg+Pythia8+Photos MC normalised to the data.

5 Backgrounds

The dominant sources of background to the $Z \rightarrow ll\gamma$ signal originate from top-quark pair production and decay with two high-p_T prompt leptons and one prompt photon in the final state and from Z+jet production with two high-p_T prompt leptons and one jet misidentified as a photon in the final state. Other smaller sources of backgrounds are also considered, such as $WZ\gamma$ production, $\tau\tau\gamma$ production with two leptonic decays of the τ-lepton, but also backgrounds with one fake or non-prompt lepton such as $W\gamma$+jet production and backgrounds from WZ production with the electron from the W-boson decay misidentified as a photon. The sum of all sources contributing to events containing two prompt leptons and one prompt photon is labelled "prompt background" and is predicted by simulation, while the sum of all other sources is labelled "fake γ background" and is estimated from data as described below. The respective contributions of these prompt and fake γ background sources to the data are listed separately with their total uncertainties for the dielectron and dimuon case in Table 1.

The overall background contribution to the signal is expected to be small, as can be seen from the small tails outside the pole region in the three-body invariant mass, $m_{ll\gamma}$, distribution of Fig. 2. A simple extrapolation from the events with large $m_{ll\gamma}$ to the signal region leads to an expectation at the percent level. The nominal method used for the background estimation in this analysis is an unbinned maximum likelihood fit of the $m_{ll\gamma}$ distribution over a wide range, $60 < m_{ll\gamma} < 120$ GeV using simulation for the prompt background sources (shape and normalisation) and also for the shape of the fake γ background. This fit is performed for each measurement bin of the differential cross-section measurements.

A cross-check of the fake γ background estimate is performed with a data-driven two-dimensional sideband method using an inverted isolation selection for the photon candidate on one side and requiring that $100 < m_{ll\gamma} < 150$ GeV on the other. This latter selection enhances the background, as shown in Fig. 2 (top). The difference between the two methods is used as an estimate of the systematic uncertainty in the fake γ background estimate. As shown in Table 1, the overall background is at the level of 2-3% of the expected signal with a total relative uncertainty of 13%.

Table 1: Total observed rates of data selected for the measurements in the $Z \rightarrow ee\gamma$ and $Z \rightarrow \mu\mu\gamma$ channels. Also shown are the expected contributions with their total uncertainties from the two main sources of background, the prompt background containing two leptons and one photon, predominantly from top-quark pair production, and the fake γ background containing two leptons and one jet misidentified as a photon, predominantly from Z+jet production (see text).

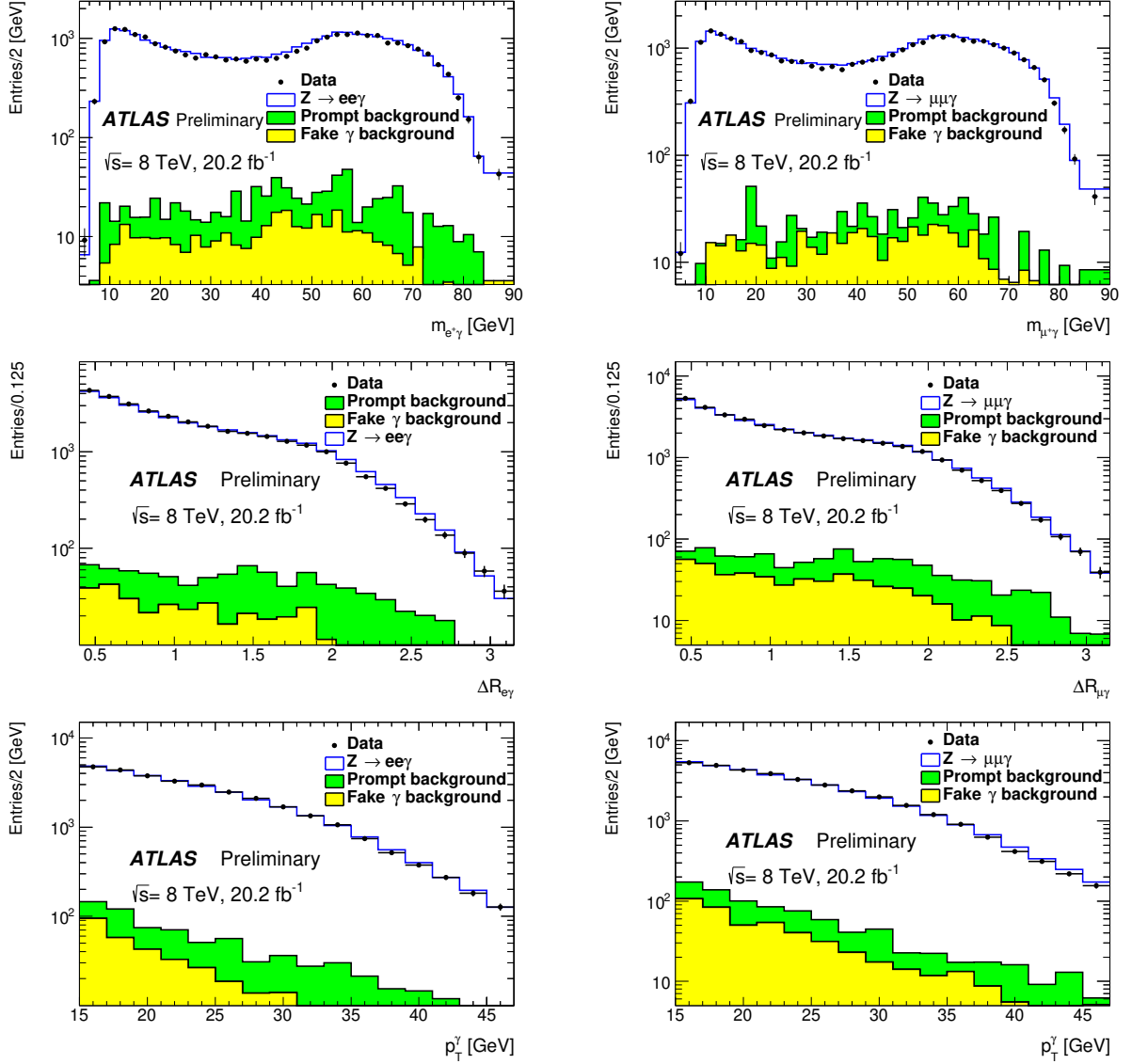| Channel	$Z \rightarrow ee\gamma$	$Z \rightarrow \mu\mu\gamma$
Data	30571	34948
Prompt background	360 ± 40	290 ± 50
Fake γ background	450 ± 90	500 ± 90
Total background	810 ± 100	790 ± 100
$Z \rightarrow ll\gamma$ expected signal	28990 ± 990	34530 ± 1100

Figure 3: For electrons (left) and muons (right), measured differential rates for $m_{l^+\gamma}$ (top), $\Delta R_{l\gamma}$ (middle), and p_T^γ (bottom). The data are shown compared to the sum of the expected contributions from the $Z \to ll\gamma$ signal, as predicted from Powheg+Pythia8+Photos, and of the prompt and fake γ backgrounds.

6 Correction for detector effects

The reconstructed differential distributions presented in Fig. 3 are corrected for detector effects and bin-to-bin migrations using an iterative Bayesian unfolding method applied to events that pass the detector-level selections. The method is applied with three iterations implemented in the RooUnfold framework [29]. The resulting unfolded distributions for the $Z \to ee\gamma$ and $Z \to \mu\mu\gamma$ signal are obtained at both bare-lepton and dressed-lepton level. Since the charged leptons and the photon are precisely measured compared to the bin sizes chosen for the differential distributions, the systematic uncertainties related to the unfolding method were found to be below 0.1%.

The particle-level selections shown in Table 2 are chosen to be as close as possible to the selections described in Section 4. The leptons and the photon are required to be prompt, meaning that they should not originate from decays of hadrons or τ-leptons. The small difference in pseudorapidity ranges for electrons and muons is retained at particle level since the electron and muon channels are not combined in this analysis (except for the low statistics $Z \to ll\gamma\gamma$ sample described in Section 9).

The response matrices, which connect the distributions at reconstruction and particle level, as well as the efficiency correction factors are derived using the Powheg+Pythia+Photos signal MC sample. The reconstruction, trigger and isolation efficiencies as well as the photon/lepton momentum scale and resolution in the MC simulation are corrected to match those determined in data. The transverse momentum distribution of the simulated $Z \to ll\gamma$ events was reweighted to that observed in data to minimise the only potentially significant bias from QCD modelling in the simulation (see Section 7 for more details).

Table 2: Fiducial volume selections for $Z \to ll\gamma$ events

Photon with $p_T > 15$ GeV
$\|\eta_\gamma\| < 2.37$ excluding $1.37 < \|\eta_\gamma\| < 1.52$
Leptons with $p_T > 25, 10$ GeV
$\|\eta_\mu\| < 2.7$
$\|\eta_e\| < 2.47$
At least one photon + one pair of same-flavour opposite-sign leptons
$\Delta R_{l\gamma} > 0.4$
$20 < m_{ll} < 80$ GeV
$80 < m_{ll\gamma} < 100$ GeV

7 Systematic uncertainties

This section describes the systematic uncertainties in the measurements of the normalised differential fiducial cross sections for the observables presented in Fig. 3. These systematic uncertainties are grouped according to their source, and their typical relative values over most of the kinematic range of the measured observables are listed in Table 3, while the relative variations of the background uncertainty and of the overall systematic uncertainty as a function of the measured observables are shown in Fig. 4, together with the variations of the statistical uncertainty in the data and of the total uncertainty in the measurements. The statistical uncertainty in the data is the dominant uncertainty over most of the measurement bins of all three observables.

The experimental systematic uncertainties in measured observables involving only leptons and photons are expected to be small, and particularly so for normalised distributions for which only the shape variations in these uncertainties remain. This can indeed be seen from Table 3 which shows contributions of at most a few per mille from the lepton/photon experimental systematic uncertainty sources. However, Fig. 4 shows that the overall systematic uncertainty is the dominant contribution at the edge of the phase space for the $m_{l^+\gamma}$ and $\Delta R_{l\gamma}$ distributions. This arises from the very limited number of simulated events in these regions which inflates the overall systematic uncertainty even though it is statistical in nature.

Table 3: Breakdown of systematic uncertainties for the normalised differential fiducial cross sections. The values shown are typical over most of the kinematic range of the unfolded observables.

Uncertainty source	$Z \to ee\gamma$ channel	$Z \to \mu\mu\gamma$ channel
Experimental		
Energy/momentum scale and resolution	0.2%	0.2%
Efficiency	0.3%	0.3%
Unfolding	< 0.1%	< 0.1%
Background subtraction	0.3%	0.3%
Theory		
PDF	< 0.1%	< 0.1%
QCD scale variations	0.1 %	0.1%
QCD modelling	0.3%	0.3%
Total	0.6%	0.6 %

Over most of the phase space of interest, one expects that the shapes of the electron and muon channels are identical, so the $e - \mu$ difference has been used as an additional cross-check of the experimental systematic uncertainties. The weighted mean of the $e - \mu$ data/MC double ratio difference was found to be -0.0011 ± 0.0085 (stat) ± 0.00007 (syst). The systematic uncertainty is reduced here purely to the contribution of the experimental systematic uncertainties which are uncorrelated between electrons and muons. The $e - \mu$ difference was thus found to be consistent with its statistical uncertainty, and no systematic trend was observed as a function of the measured differential distributions.

Table 3 shows that the theoretical uncertainties from QCD scale variations and PDFs, related to the acceptance of the photon/lepton fiducial cuts, are very small, at the per mil level, as expected. However, any QCD-related mis-modelling of Z-boson production not covered by these uncertainties may have a significant and direct impact on the QED-related observables of interest. As mentioned above, the simulated events were reweighted to reproduce the observed transverse momentum spectrum of $Z \to ll\gamma$ decays. This has potentially a direct impact on the photon transverse momentum spectrum, but it also affects at the percent level certain regions of phase space for the $m_{l^+\gamma}$ and $\Delta R_{l\gamma}$ distributions (the most significant impact has been observed in the case of the Sherpa 1.4 predictions). After this reweighting procedure, the residual QCD modelling systematic uncertainties were found to be very small, at the few per mil level. This was further verified by reweighting to data also the other kinematic observables related to Z-boson production, namely the Z-boson rapidity and the angular coefficients related to the lepton kinematics in the rest-frame of the Z-boson. As a final cross-check, the Sherpa 1.4 predictions for the reconstructed observables, after reweighting to the observed transverse momentum spectrum of $Z \to ll\gamma$ decays, were unfolded using the nominal Powheg+Pythia+Photos MC. The resulting systematic uncertainty, as derived from the difference between the generator-level Sherpa 1.4 prediction and that obtained after this unfolding cross-check, was found to be negligible, i.e. below the per mille level.
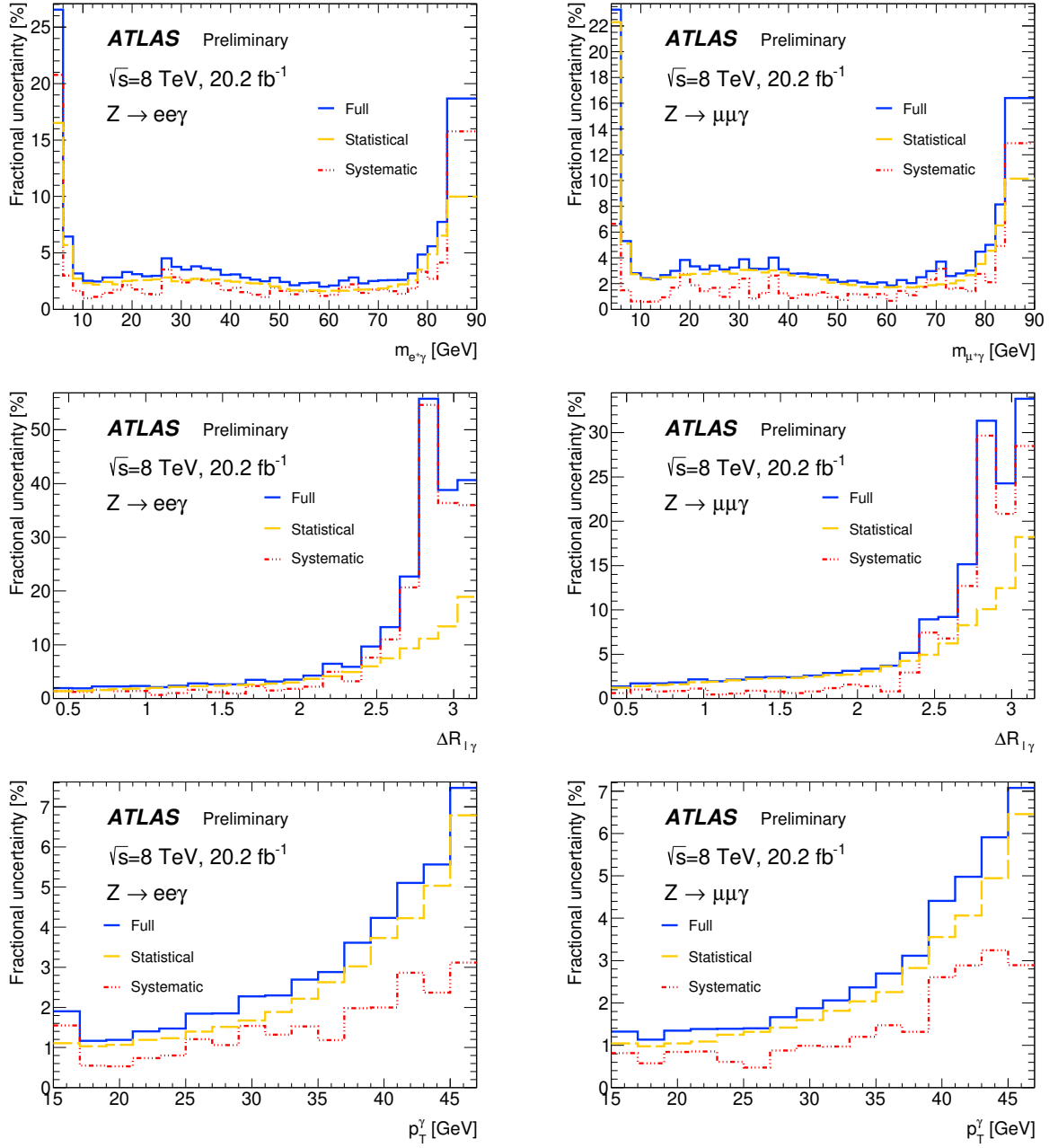
Figure 4: Breakdown of relative uncertainties for the normalised unfolded differential cross sections as a function of the observables of interest, $m_{l^+\gamma}$ (top), $\Delta R_{l\gamma}$ (middle), and p_T^γ (bottom), shown separately for the $Z \to ee\gamma$ (left) and $Z \to \mu\mu\gamma$ (right) channels.

8 Results for $Z \rightarrow ll\gamma$ process

8.1 Differential cross-sections

The measurement results are presented here as unfolded normalised differential cross-sections for the three observables of interest, namely the invariant mass of the positively charged lepton and the photon, $m_{l^+\gamma}$, the angular distance, $\Delta R_{l\gamma}$, between the photon and the closer of the two leptons, and the transverse momentum, p_T^γ, of the photon. These differential cross-sections are normalised to the total measured fiducial cross section to minimise the experimental uncertainties and also to remove potentially dominant QCD-related theoretical uncertainties when comparing to predictions. The results below are shown separately for the electron and muon channels in the case of bare leptons. This maximises the sensitivity to expected small differences in the distributions between the two lepton flavours (see Figure 1).

Figure 5 shows in the case of bare leptons, separately for the electron and muon channels, the unfolded normalised differential distributions for the data with their uncertainties compared to the predictions with uncertainties from Powheg+Pythia8+Photos, Sherpa 2.2.4 (YFS), and KKMChh. As discussed in Section 3, Powheg+Pythia8+Photos considers only QED FSR and has an associated theoretical uncertainty of 0.2% obtained by varying the configuration of Photos from its default one to the slightly less precise prediction not including the Z-boson matrix-element correction discussed in Section 3. When quoting such a small uncertainty, one has to assume of course that the contributions from QED ISR and from IFI are even smaller. The combined QED ISR/IFI contribution in the fiducial region of the analysis presented in this note has been estimated with KKMChh to be 3×10^{-3} for the integrated fiducial cross-sections, with an uncertainty below 10^{-3}. These results have been confirmed using the CompHEP [30] code. In the case of the Sherpa 2.2.4 predictions which are also shown in Fig. 5, the uncertainty band is much larger and probably over-conservative, about 2%. This was estimated using a recipe similar to that described in [31], corresponding to higher-order QED corrections which are only known at the Z-boson pole and assumed to be potentially not applicable outside the pole region.

The agreement between the measurements and the predictions from the MC simulations is reasonable for all three distributions over most of their range, both for electrons and muons. The agreement between the predictions themselves is better for $m_{l^+\gamma}$ than their respective agreement with the data, suggesting perhaps that most of the fluctuations seen in the ratio plots for this observable are related to statistical fluctuations in the data since they are limited to a few bins. However, there is a noticeable discrepancy between the measurement in the electron channel and the Powheg+Pythia8+Photos prediction for large values of $\Delta R_{l\gamma}$ at the edge of the phase space where the two leptons from Z-boson decay recoil against the photon.
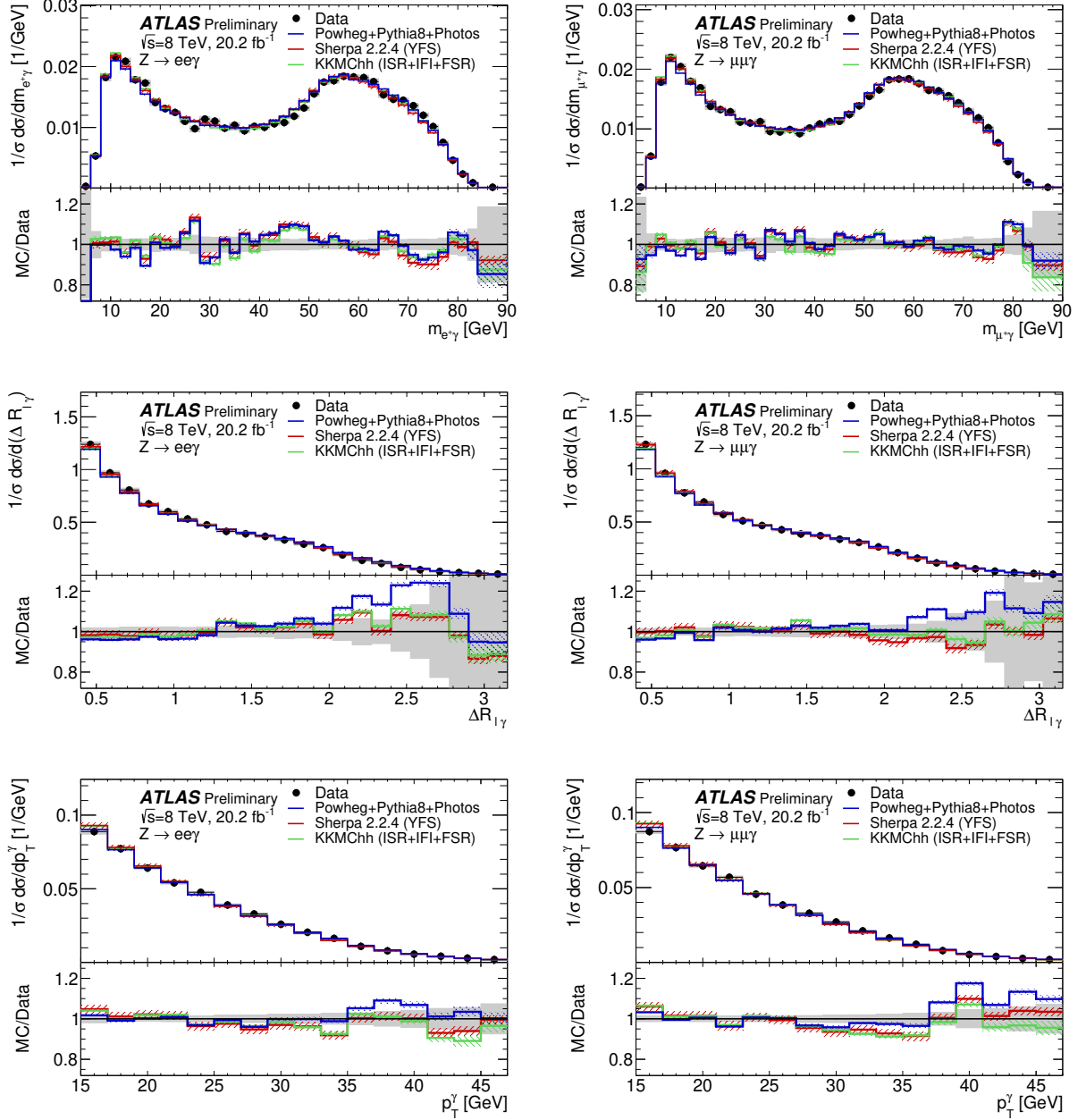
Figure 5: Unfolded normalised differential fiducial cross sections for the $Z \to ee\gamma$ (left) and $Z \to \mu\mu\gamma$ (right) channels. The results are shown in the case of bare leptons for the $m_{l^+\gamma}$ (top), $\Delta R_{l\gamma}$ (middle), and p_T^γ (bottom) distributions. The data are compared to the predictions from Powheg+Pythia8+Photos, Sherpa 2.2.4, and KKMChh. The bottom panels represent the ratios of these predictions to the data, where the gray band around unity represents the total data uncertainties and the dashed lines around the predictions represent their respective total uncertainties (see text).

Table 4: Uncertainties in the integrated fiducial cross-section measurements. The values for bare leptons with $m_{ll} > 20$ GeV are shown.

Uncertainty	$Z \rightarrow ee\gamma$	$Z \rightarrow \mu\mu\gamma$
Statistical	0.7%	0.7%
Experimental systematic	3.5%	2.3%
Luminosity	1.9%	1.9%
QCD theory	0.3%	0.3%
Total	4.1%	3.1 %

Table 5: Integrated fiducial cross sections (pb) for three ranges of the dilepton mass m_{ll}. The measurements are presented for bare leptons with the breakdown of their uncertainties together with the predictions from Powheg+Pythia8+Photos normalised as described in the text.

Cross-sections in pb	Measurement	Prediction
$Z \rightarrow ee\gamma$ ($20 < m_{ll} < 80$ GeV)	3.03 ± 0.02 (stat) ± 0.11 (syst) ± 0.06 (lumi)	2.94 ± 0.10
$Z \rightarrow \mu\mu\gamma$ ($20 < m_{ll} < 80$ GeV)	3.17 ± 0.02 (stat) ± 0.07 (syst) ± 0.07 (lumi)	3.20 ± 0.10
$Z \rightarrow ee\gamma$ ($45 < m_{ll} < 80$ GeV)	2.70 ± 0.02 (stat) ± 0.10 (syst) ± 0.06 (lumi)	2.61 ± 0.10
$Z \rightarrow \mu\mu\gamma$ ($45 < m_{ll} < 80$ GeV)	2.84 ± 0.02 (stat) ± 0.06 (syst) ± 0.06 (lumi)	2.84 ± 0.10
$Z \rightarrow ee\gamma$ ($20 < m_{ll} < 45$ GeV)	0.326 ± 0.005 (stat) ± 0.011 (syst) ± 0.006 (lumi)	0.335 ± 0.01
$Z \rightarrow \mu\mu\gamma$ ($20 < m_{ll} < 45$ GeV)	0.321 ± 0.005 (stat) ± 0.006 (syst) ± 0.006 (lumi)	0.355 ± 0.01

8.2 Integrated fiducial cross sections

The normalised differential fiducial cross-section measurements presented above are only sensitive to the shape of the distributions, but benefit from cancellations of experimental systematic uncertainties for the sources which do not vary much with lepton p_{T}, such as the lepton efficiencies. This section presents the integrated fiducial cross-section measurements in the electron and muon channels and discusses the results for three different ranges of the dilepton mass. The uncertainties in the integrated fiducial cross sections are summarised in Table 4. They include the uncertainty of 1.9% in the integrated luminosity and are somewhat larger for some of the experimental sources than those listed in more detail in Table 3 for the reasons explained above.

The comparisons between the measured integrated cross sections over three different dilepton mass ranges and the corresponding theory predictions, normalised to the QCD NNLO prediction used in [32] for the total inclusive cross section for Z-boson production, are presented in Table 5. The agreement between the measurements and the predictions is reasonable within their comparable overall uncertainties. The uncertainties in the theory predictions are also taken from [32]. As explained in Section 1 and shown in Table 5 for the theory predictions, the cross sections for the $Z \rightarrow \mu\mu\gamma$ process are expected to be larger than those for the $Z \rightarrow ee\gamma$ process. This difference is enhanced significantly in this measurement by

Table 6: Fiducial volume selections for $Z \to ll\gamma\gamma$ events

Two photons with $p_T > 15$ and 10 GeV, respectively
$|\eta_\gamma| < 2.37$ excluding $1.37 < |\eta_\gamma| < 1.52$
Two same-flavour opposite-sign leptons with $p_T > 25, 15$ GeV
$|\eta_\mu| < 2.7$
$|\eta_e| < 2.47$
$\Delta R_{l\gamma} > 0.4$ for both photons
$m_{ll\gamma} < 80$ GeV for both photons

the higher acceptance, due to the pseudorapidity selection, of the $Z \to \mu\mu\gamma$ channel with respect to the $Z \to ee\gamma$ channel.

9 First measurement of the $Z \to ll\gamma\gamma$ process

This section presents a first measurement of the $Z \to ll\gamma\gamma$ process at the LHC. Given the limited statistics expected for the dataset considered here, the candidate event samples for each charged lepton flavour were combined together and the selection requirements on the sub-leading photon were loosened with respect to the leading one. The sample considered was the same one as for the $Z \to ll\gamma$ analysis in terms of the charged lepton requirements, with however a tighter selection requirement of $p_T > 15$ GeV for the softer of the two leptons, but without any requirement on the dilepton mass. The two photons were required to be within the same pseudorapidity range as for the $Z \to ll\gamma$ analysis with thresholds in p_T set to respectively 15 and 10 GeV and within an angular distance, $\Delta R_{l\gamma}$ of at least 0.4 from each charged lepton. Figure 6 (top left) shows the invariant mass of the two leptons and the two photons, $m_{ll\gamma\gamma}$, versus the invariant mass of the two leptons and of the highest p_T photon, $m_{ll\gamma}$. As illustrated in this figure, for values of $m_{ll\gamma}$ larger than 80 GeV, significant contributions of background from $Z \to ll\gamma$ +jet(s) events and from $Z \to \ell\ell$ +jets events are expected.

In order to reduce these contributions and also possible contributions from $Z \to ll\gamma$ events with initial state QED radiation to the percent level or less, the invariant mass, $m_{ll\gamma}$, was required to be below 80 GeV for both photons. These requirements are summarised as fiducial volume selections in Table 6. A total of 116 events, corresponding to 61 electron pairs and 55 muon pairs, were thus selected as $Z \to ll\gamma\gamma$ candidates. The dominant background from $Z \to ll\gamma$+jet events was estimated by applying the same two-dimensional sideband method as that described for the main analysis: the quality and isolation criteria were inverted for the second photon. The background was found to be less than one event and Fig. 6 (top right) illustrates this through the observed distribution of $m_{ll\gamma\gamma}$ which displays no events outside the pole region.

The data were compared to MC $Z \to ll\gamma\gamma$ samples produced using the same Powheg+Pythia8+Photos version used for the main analysis and Sherpa 1.4 $ME_{\gamma\gamma}$ (see Section 3). Figure 6 (top right, middle and bottom) show that both MC predictions describe the data within the large statistical uncertainties for a selection of observables.

Finally, the data were corrected for detector efficiencies and resolution and fiducial cross sections were extracted together with unfolded distributions of several observables. The fiducial cross section is measured to be 16.1 ± 1.6 (stat) ± 0.5 (syst) fb for bare leptons and 16.3 ± 1.6 (stat) ± 0.4 (syst) fb for dressed leptons. The expected fiducial cross sections from Powheg+Pythia8+Photos and Sherpa 1.4 $ME_{\gamma\gamma}$ are 7.74 ± 1.26 (stat) fb and 6.06 ± 0.10 (stat) fb respectively. Figure 7 shows the unfolded distributions for the data compared to the predictions. The uncertainties shown are the combined statistical and systematic uncertainties for the data and only the statistical uncertainties for the predictions. The agreement between data and predictions is reasonable within the uncertainties of this first measurement for the unfolded normalised differential distributions. The fiducial cross-section predictions are however significantly below the measured cross section.
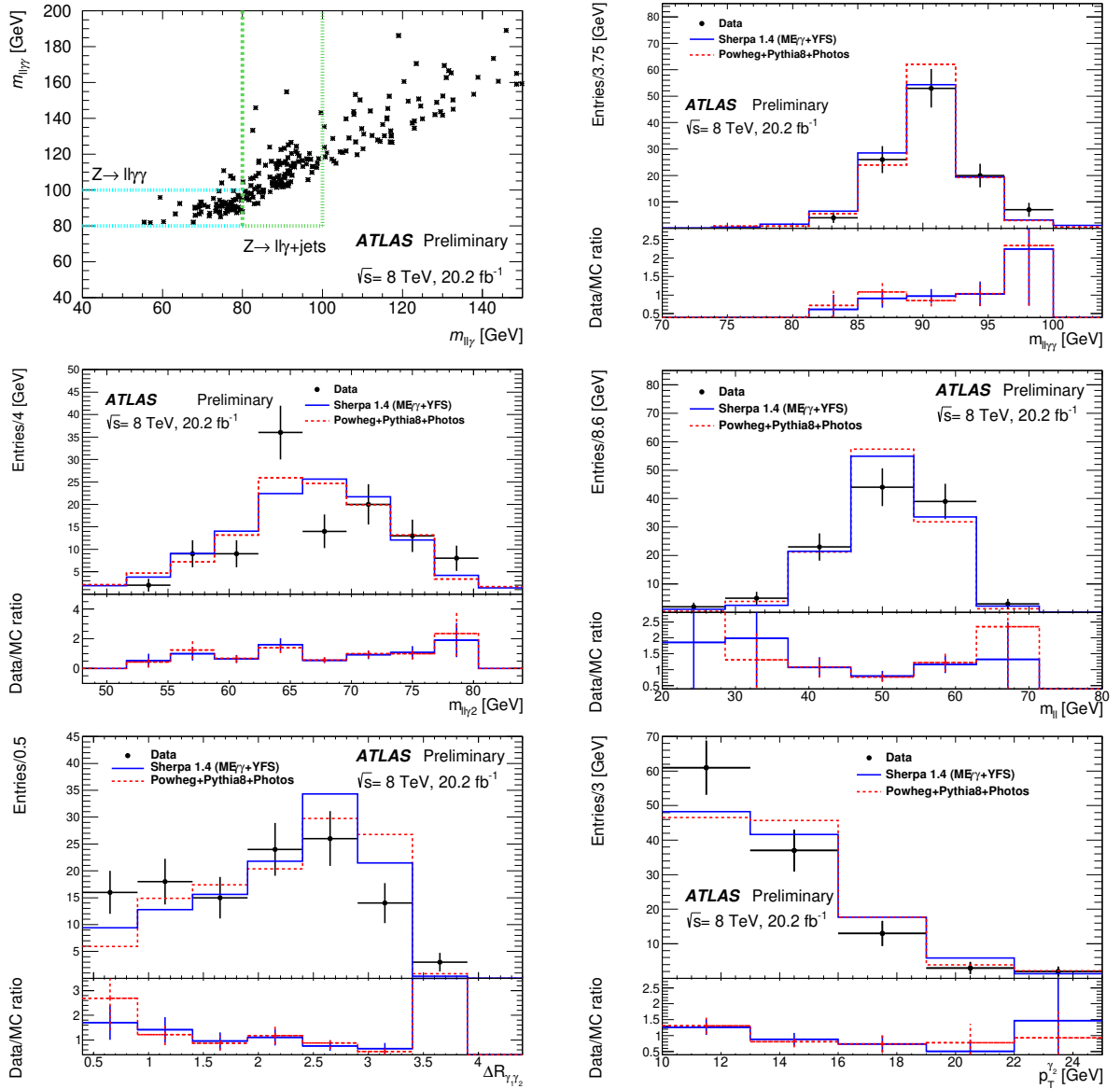
Figure 6: For all selected $Z \rightarrow ll\gamma\gamma$ candidates before applying any selection on the invariant mass of the two leptons and each photon described in the text, distribution of invariant mass of the two leptons and the two photons, $m_{ll\gamma\gamma}$ versus the invariant mass of the two leptons and of the highest p_T photon, $m_{ll\gamma}$ (top left). The horizontal dashed (blue) rectangle indicates the region where the $Z \rightarrow ll\gamma\gamma$ signal is expected and the vertical dashed (green) rectangle indicates the region dominated by background from $Z \rightarrow ll\gamma$ events accompanied by one or more jets. Also shown after all selection requirements are the distributions of the total invariant mass (top right), of the invariant mass of the two leptons and the second photon, of the dilepton mass, of the angular distance between the two photons, and of the transverse momentum of the second photon. The data are compared to predictions from Powheg+Pythia8+Photos and Sherpa 1.4 ME$_{\gamma\gamma}$, normalised both to the data. The results are shown for bare leptons, and electrons and muons have been combined. The uncertainties shown are statistical.
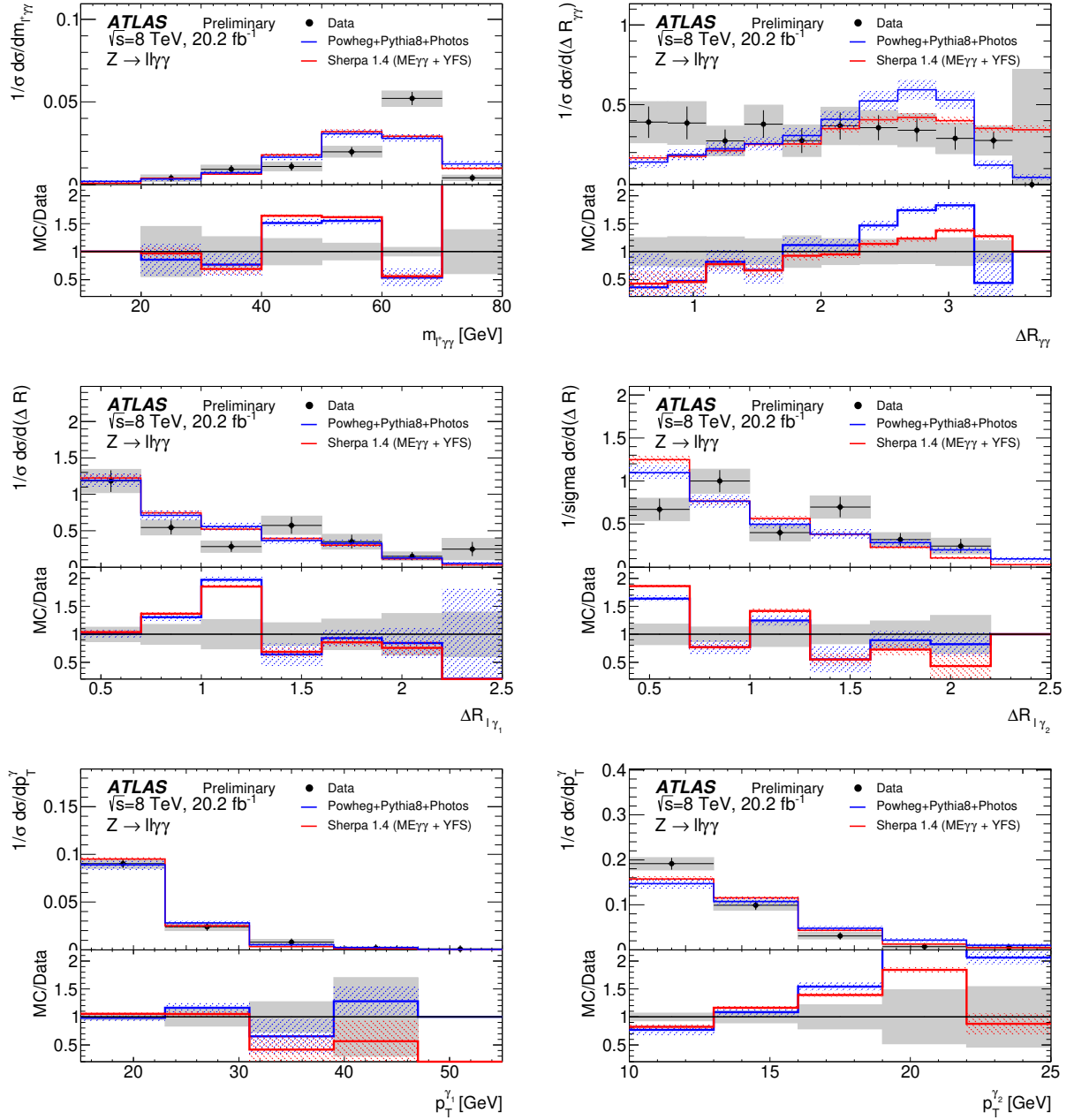
Figure 7: For all selected $Z \to ll\gamma\gamma$ candidates, unfolded normalised distributions of $m_{l^+\gamma\gamma}$ (top left), of $\Delta R_{\gamma\gamma}$ (top right), of the angular distance between the first (middle left) and second (middle right) photon and the closest lepton, and of the transverse momentum spectrum of the two photons (bottom). The unfolded data are compared to predictions from Powheg+Pythia8+Photos and Sherpa 1.4 $ME_{\gamma\gamma}$. The results are shown for bare leptons, and electrons and muons have been combined. The uncertainties shown are the combined statistical and systematic uncertainties for the data and only the statistical uncertainties, which are dominant, for the predictions.

10 Conclusions

This note presents the first ATLAS measurement of unfolded normalised differential fiducial cross sections for $Z \rightarrow ee\gamma$ and $Z \rightarrow \mu\mu\gamma$ final states together with a few integrated fiducial cross-sections. The overall accuracy of the measurements is at the 1-2% percent level over a large fraction of the overall phase space, with an average overall systematic uncertainty of 0.6% for the chosen observables, $m_{l^+\gamma}$, $\Delta R_{l\gamma}$, and p_T^{γ}.

The results are in agreement with predictions of MC generators containing state-of-the-art QED FSR calculations such as Photos (in PowHeg+Pythia8+PHOTOS) and YFS (in Sherpa 2.2.4). They are also in agreement with the recent calculations of KKMChh which provides a consistent and gauge-invariant breakdown of the different contributions to final states containing two charged leptons and a high-p_T photon, and thus demonstrates that the QED ISR and IFI contributions are very small for the fiducial selections of the analysis described in this note.

Finally, the $Z \rightarrow ll\gamma\gamma$ process has been observed for the first time and is described within its present large statistical uncertainties by the available calculations in terms of the shapes of the various distributions. The measured integrated cross section is however significantly larger than the predictions.

References

[1] ATLAS Collaboration,
Measurement of the W-boson mass in pp collisions at $\sqrt{s}$ = 7 TeV with the ATLAS detector,
Eur. Phys. J. C **78** (2018) 110, [Erratum: Eur.Phys.J.C 78, 898 (2018)],
arXiv: 1701.07240 [hep-ex].

[2] ATLAS Collaboration, *Measurement of the effective leptonic weak mixing angle using electron and muon pairs from Z-boson decay in the ATLAS experiment at $\sqrt{s}$ = 8 TeV*, (2018), URL: https://cds.cern.ch/record/2630340/files/ATLAS-CONF-2018-037.pdf?version=1.

[3] S. Jadach, B. Ward and Z. Was,
Coherent Exclusive Exponentiation For Precision Monte Carlo Calculations,
Phys. Rev. D **63** (11 2001) 3009,
URL: https://journals.aps.org/prd/pdf/10.1103/PhysRevD.63.113009.

[4] P. Golonka and Z. Was, *Next to Leading Logarithms and the PHOTOS Monte Carlo*,
Eur.Phys.J. **C50** (2007) 53.

[5] D. Yennie, S. Frautschi and H. Suura,
The infrared divergence phenomena and high-energy processes, Annals of Physics **13** (1961) 379.

[6] P. Nason, *A New method for combining NLO QCD with shower Monte Carlo algorithms*,
JHEP **11** (2004) 040.

[7] S. Frixione, P. Nason and C. Oleari,
Matching NLO QCD computations with parton shower simulations: the POWHEG method,
JHEP **11** (2007) 070, arXiv: 0709.2092 [hep-ph].

[8] S. Alioli, P. Nason, C. Oleari and E. Re, *A general framework for implementing NLO calculations in shower Monte Carlo programs: the POWHEG BOX*, JHEP **06** (2010) 043,
arXiv: 1002.2581 [hep-ph].

[9] S. Alioli, P. Nason, C. Oleari and E. Re,
NLO vector-boson production matched with shower in POWHEG, JHEP **07** (2008) 060,
arXiv: 0805.4802 [hep-ph].

[10] T. Gleisberg et al., *Event generation with SHERPA 1.1*,
Journal of High Energy Physics **2009** (2009) 007.

[11] E. Bothmann et al., *Event Generation with Sherpa 2.2*, SciPost Phys. **7** (2019) 034,
arXiv: 1905.09127 [hep-ph].

[12] ATLAS Collaboration, *The ATLAS experiment at the CERN Large Hadron Collider*,
JINST **3** (2008) S08003.

[13] J. Pumplin et al.,
New Generation of Parton Distributions with Uncertainties from Global QCD Analysis,
Journal of High Energy Physics **2002** (2002) 012,
URL: %7Bhttps://doi.org/10.1088/1126-6708/2002/07/012%7D.

[14] T. Sjöstrand, S. Mrenna and P. Skands, *A brief introduction to PYTHIA 8.1*,
Comput. Phys. Commun. **178** (2008) 852, arXiv: 0710.3820 [hep-ph].

[15] ATLAS Collaboration, *Summary of ATLAS Pythia 8 tunes*, ATL-PHYS-PUB-2012-003, 2012,
URL: https://cds.cern.ch/record/1474107.

[16] N. Davidson, T. Przedzinski and Z. Was,
PHOTOS interface in C++: Technical and physics documentation,
Comput. Phys. Commun. **199** (2016) 86, arXiv: 1011.0937 [hep-ph].

[17] H.-L. Lai et al., *New parton distributions for collider physics*, Phys. Rev. D **82** (7 2010) 074024,
URL: https://link.aps.org/doi/10.1103/PhysRevD.82.074024.

[18] S. Jadach, B. F. L. Ward, Z. A. Was and S. A. Yost,
KK MC-hh: Resummed exact $O(\alpha^2 L)$ EW corrections in a hadronic MC event generator,
Phys. Rev. D **94** (7 2016) 074006,
URL: https://link.aps.org/doi/10.1103/PhysRevD.94.074006.

[19] S. Jadach, B. F. L. Ward, Z. A. Was and S. A. Yost, *KK MC-hh: Systematic studies of exact $O(\alpha^2 L)$
CEXX EW corrections in a hadronic MC for Precision Z/γ^* Physics at LHC Energies*, Phys. Rev. D
99 (7 2019) 076016, [We are very grateful to S. Yost for providing the calculations from KKMChh.],
URL: https://link.aps.org/doi/10.1103/PhysRevD.99.076016.

[20] S. Hoeche, F. Krauss, M. Schonherr and F. Siegert,
QCD matrix elements + parton showers: The NLO case, JHEP **04** (2013) 027.

[21] ATLAS Collaboration, *The ATLAS Simulation Infrastructure*, Eur. Phys. J. C **70** (2010) 823,
arXiv: 1005.4568 [physics.ins-det].

[22] S. Agostinelli et al., *GEANT4 – a simulation toolkit*, Nucl. Instrum. Meth. A **506** (2003) 250.

[23] ATLAS Collaboration, *Electron and photon performance measurements with the ATLAS detector
using the 2015–2017 LHC proton–proton collision data*, JINST **14** (2019) P12006,
arXiv: 1908.00005 [hep-ex].

[24] ATLAS Collaboration, *Muon reconstruction performance of the ATLAS detector in proton–proton
collision data at $\sqrt{s}$ = 13 TeV*, Eur. Phys. J. C **76** (2016) 292, arXiv: 1603.05598 [hep-ex].

[25] ATLAS Collaboration,
Topological cell clustering in the ATLAS calorimeters and its performance in LHC Run 1,
Eur. Phys. J. C **77** (2017) 490, arXiv: 1603.02934 [hep-ex].

[26] M. Cacciari, G. P. Salam and G. Soyez, *The catchment area of jets*, JHEP **04** (2008) 005,
arXiv: 0802.1188 [hep-ph].

[27] M. Cacciari, G. P. Salam and S. Sapeta, *On the characterisation of the underlying event*,
JHEP **04** (2010) 065, arXiv: 0912.4926 [hep-ph].

[28] ATLAS Collaboration, *Measurement of the inclusive isolated prompt photon cross section in pp
collisions at $\sqrt{s}$ = 7 TeV with the ATLAS detector*, Phys. Rev. D **83** (2011) 052005,
arXiv: 1012.4389 [hep-ex].

[29] T. Adye, *Unfolding algorithms and tests using RooUnfold*,
(2011) 313, Comments: 6 pages, 5 figures, presented at PHYSTAT 2011, CERN, Geneva,
Switzerland, January 2011, to be published in a CERN Yellow Report, arXiv: 1105.1160,
URL: https://cds.cern.ch/record/1349242.

[30] E. Boos et al., *CompHEP 4.4—automatic computations from Lagrangians to events*,
Nuclear Instruments and Methods in Physics Research Section A: Accelerators, Spectrometers,
Detectors and Associated Equipment **534** (2004) 250, Proceedings of the IXth International
Workshop on Advanced Computing and Analysis Techniques in Physics Research, ISSN: 0168-9002,
URL: https://www.sciencedirect.com/science/article/pii/S0168900204015402.

[31] C. Gütschow and M. Schönherr, *Four lepton production and the accuracy of QED FSR*,
Eur. Phys. J. C **81** (2021) 48, URL: https://doi.org/10.1140/epjc/s10052-020-08816-9.

[32] ATLAS Collaboration, *Measurements of top-quark pair to Z-boson cross-section ratios at*
$\sqrt{s} = 13, 8, 7$ *TeV with the ATLAS detector*, JHEP **02** (2017) 117, arXiv: 1612.03636 [hep-ex].

Appendix

This Appendix presents two additional figures as supplementary material to the note itself. Figure 8 displays the MC predictions from Powheg+Pythia8+Photos, Sherpa 2.2.4 (YFS), and KKMChh, as shown in Fig. 5, but without any comparison to data, such that the three calculations can be compared to each other without any impact from fluctuations in the data. The calculations from the nominal Powheg+Pythia8+Photos MC are used as the reference for the ratio panel at the bottom of each plot. Figure 9 displays for each of the normalised differential distributions measured for the $Z \to ll\gamma$ events the shapes predicted by the full KKMChh calculation, which includes the dominant QED FSR contribution (also shown separately in the top panels) and the very small contributions from QED ISR and IFI. The bottom panels show that the sum of these latter contributions are compatible with zero within their statistical uncertainties and do not display any trend above the percent level over the whole kinematic range explored.
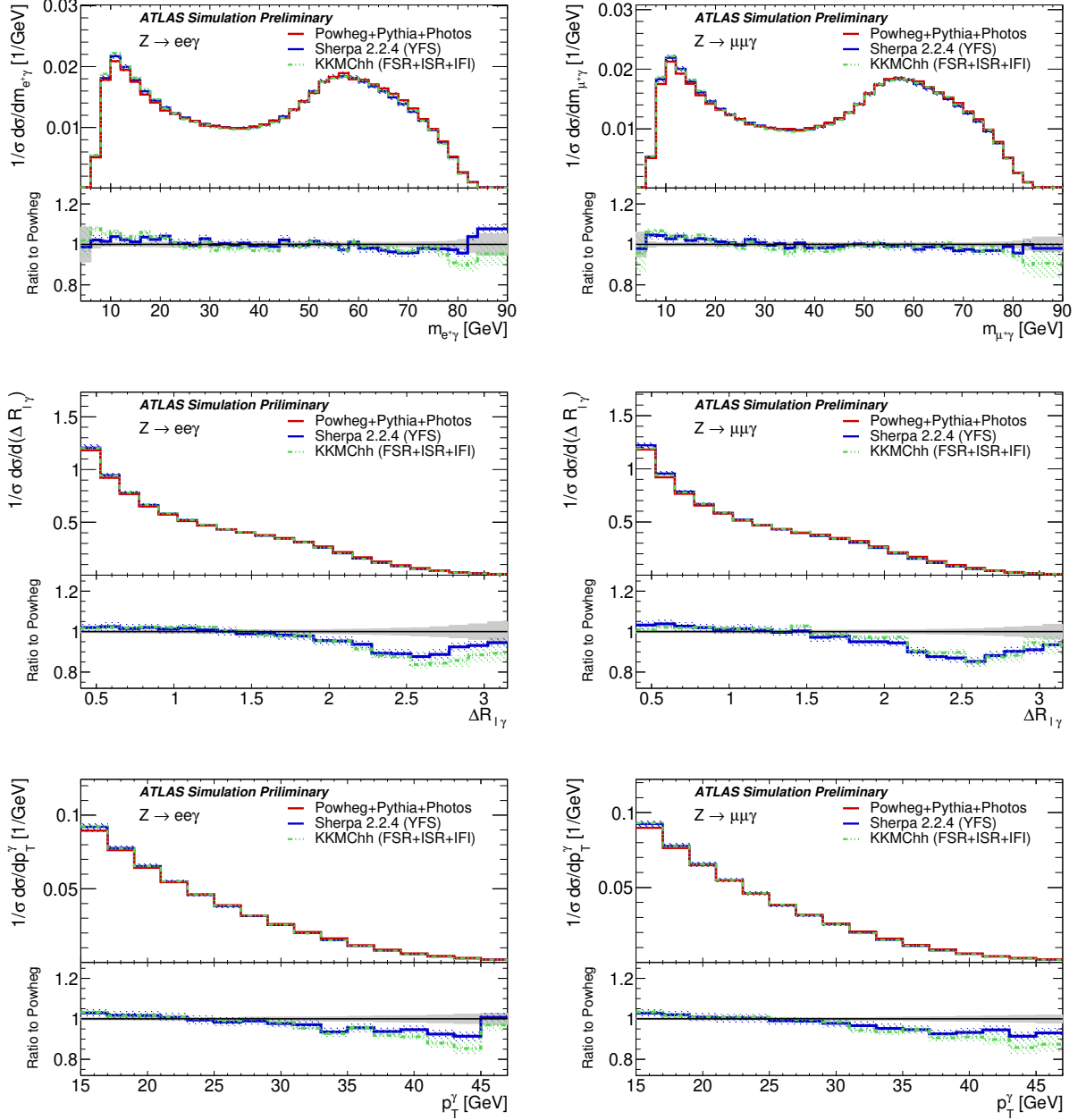
Figure 8: Normalised differential fiducial cross sections for the $Z \rightarrow ee\gamma$ (left) and $Z \rightarrow \mu\mu\gamma$ (right) channels. The results are shown in the case of bare leptons for the $m_{l^+\gamma}$ (top), $\Delta R_{l\gamma}$ (middle), and p_T^γ (bottom) distributions. The predictions from Powheg+Pythia8+Photos, Sherpa 2.2.4 (YFS), and KKMChh are shown with their respective total uncertainties (see Section 8). The bottom panels represent the ratios of the Sherpa 2.2.4 (YFS) and KKMChh predictions to those from the nominal Powheg+Pythia8+Photos MC, where the gray band around unity represents the total uncertainty from Powheg+Pythia8+Photos.
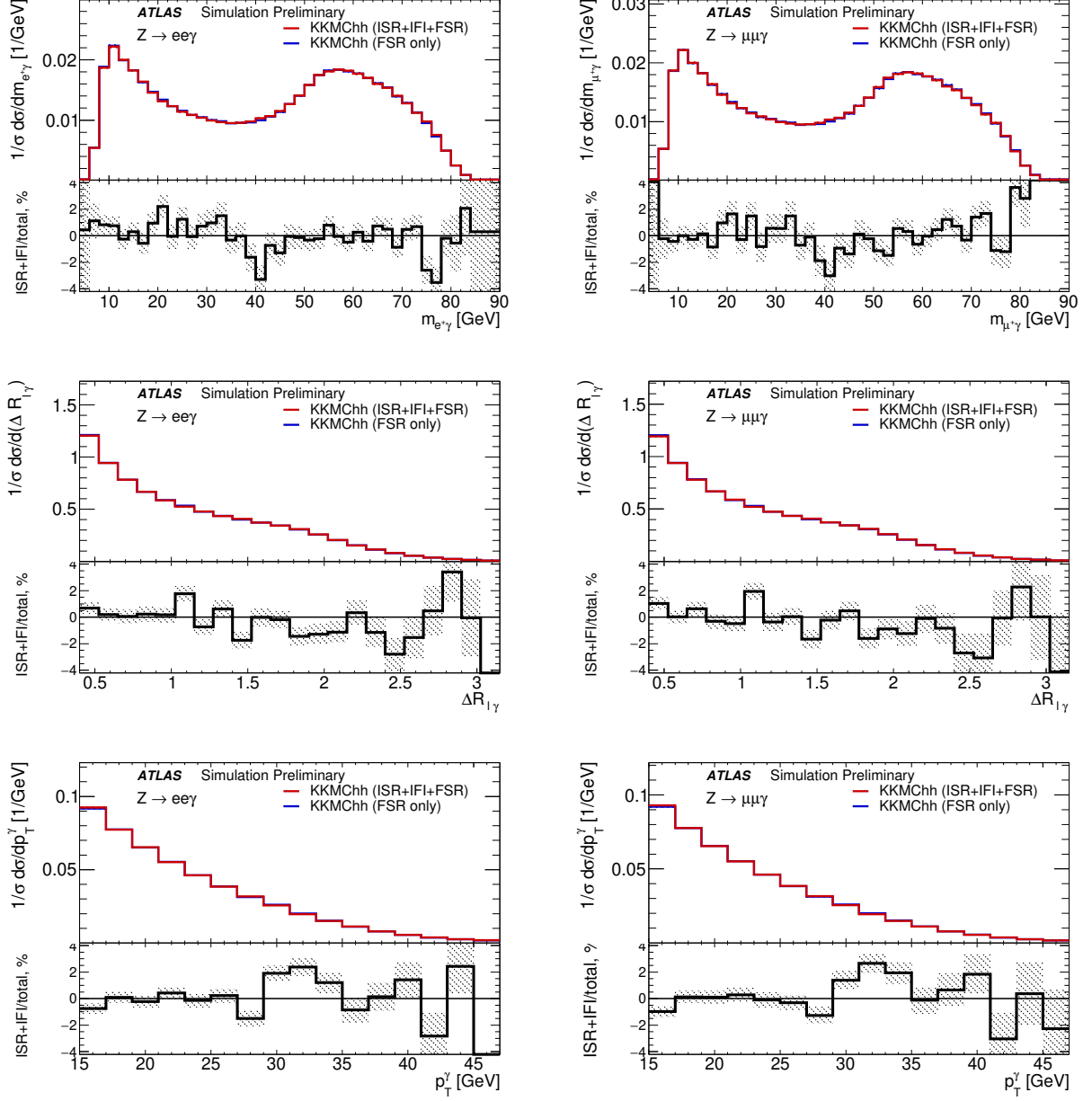
Figure 9: Expected contributions of QED FSR and full QED (ISR+IFI+FSR) KKMChh predictions for the normalised differential spectra of $m_{l^+\gamma}$, $\Delta R_{l\gamma}$, and p_T^γ. The predictions are shown for bare leptons and the bottom panels show how small the QED ISR+IFI contribution is with respect to the total. The integrated contribution is approximately 3×10^{-3} in the phase space of the measurements.